On-chip Thermometry for Microwave Optomechanics Implemented in a Nuclear Demagnetization Cryostat

X. Zhou,[1,2] D. Cattiaux,[1] R. R. Gazizulin,[1] A. Luck,[1] O. Maillet,[1] T. Crozes,[1] J.-F. Motte,[1] O. Bourgeois,[1] A. Fefferman,[1] and E. Collin[1,*]

[1]*Univ. Grenoble Alpes, Institut Néel - CNRS UPR2940, 25 rue des Martyrs, BP 166, Grenoble Cedex 9 38042, France*

[2]*Since 01/10/2017: IEMN, Univ. Lille - CNRS UMR8520, Av. Henri Poincaré, Villeneuve d'Ascq 59650, France*

We report on microwave optomechanics measurements performed on a nuclear adiabatic demagnetization cryostat, whose temperature is determined by accurate thermometry from below 500 μK to about 1 K. We describe a method for accessing the on-chip temperature, building on the blue-detuned parametric instability and a standard microwave setup. The capabilities and sensitivity of both the experimental arrangement and the developed technique are demonstrated with a very weakly coupled silicon-nitride doubly clamped beam mode of about 4 MHz and a niobium on-chip cavity resonating around 6 GHz. We report on an unstable intrinsic driving force in the coupled microwave-mechanical system acting on the mechanics that appears below typically 100 mK. The origin of this phenomenon remains unknown, and deserves theoretical input. It prevents us from performing reliable experiments below typically 10–30 mK; however *no evidence* of thermal decoupling is observed, and we propose that the same features should be present in *all devices* sharing the microwave technology, at different levels of strengths. We further demonstrate empirically how most of the unstable features can be annihilated, and speculate how the mechanism could be linked to atomic-scale two-level systems. The described microwave and microkelvin facility is part of the European Microkelvin Platform, and shall be used for further experiments within and *below* the millikelvin range.

I. INTRODUCTION

Advances in clean-room technologies within the last decades make it possible to create mechanical elements with one (or more) dimensions below a micron, namely nanoelectromechanical systems (NEMS) [1]. These objects can be embedded in electronic circuits, and today even within *quantum* electronic circuits [2–4]. Indeed a breakthrough has been made with microwave optomechanics, essentially shifting the concepts of optomechanics into the microwave domain [5]. These quantum-*mechanical* devices can then be thought of as a new resource for quantum electronics and quantum-information processing, with the realization of, e.g., quantum-limited optical-photon to microwave-photon converters and nonreciprocal microwave circuits [6–11]. Profound quantum concepts are also under study, with, for instance, mechanical motion squeezing [12] and recently mechanical entanglement of *separate* objects [13].

In order to operate at the quantum limit, the mechanical mode in use has to be initially in its quantum ground state;

for experiments on microwave optomechanics based on megahertz motion, this shall rely on a strong red-detuned pump signal that *actively* cools the mode, with an environment remaining "hot" [10,14,15]. For most applied issues this is not a problem, even if it brings an additional complexity with a microwave tone that has to be kept on, which could lead to heating of the circuit and mixing with other signals involved. However, for all experiments aiming at a careful characterization of the mechanical decoherence due to the thermal bath, this is impractical: the whole system is required to be in thermodynamic equilibrium. As such, theoretical proposals testing the grounds of quantum mechanics have been released in the literature, both on microwave setups using quantum circuits [16] and conventional optomechanics (i.e., with lasers) [17].

Indeed, the first attempt to use nuclear adiabatic demagnetization for optomechanics is due to Dirk Bouwmeester, building on the technology of Leiden Cryogenics [18]. This ambitious setup was aimed at cooling a *macroscopic* moving mirror actuated and detected by optical means. On the other hand, a microwave-based optomechanical system hosting a NEMS is much less demanding; the heat loads

---

*eddy.collin@grenoble.cnrs.fr

from both the photon field and the internal heat release of materials are much less. As such, these setups have already proven to be compatible with dilution (millikelvin) technology [2–5,10,12,13].

We thus build a microwave platfrom for optomechanics on a nuclear adiabatic demagnetization cryostat. The microwave circuitry is kept as basic as possible so far for demonstration purposes; no Josephson parametric amplifier (JPA) is used, and we rely only on *intrinsic* properties of optomechanics for the measurement [19]. The cryostat reaches temperatures below 500 μK, and is equipped with accurate thermometry from the lowest temperatures up to about 1 K: using a noise superconducting quantum interference device (SQUID)-based thermometer [20] plus a ^{3}He-fork thermometer [21].

We report on measurements realized on this platform with a very weakly coupled doubly clamped beam flexural mode embedded in an on-chip cavity. Beam-based devices are indeed a tool of choice for applications like ultimate sensing (e.g., single-molecule mass spectrometry [22]), while the smallness of the photon-phonon coupling enables demonstrating the sensitivity of the methods used: we build on the optomechanical blue-detuned pumping instability to extract the *on-chip* temperature. On the other hand, popular drumhead devices achieve routinely much higher couplings [3,12] (from $\times 10$ to $\times 100$); the very same methods can then be applied with much less power, therefore limiting heating problems. We report not only on the thermalization of the mechanical mode itself, but also on the bulk of the mechanical element with the temperature of its constitutive two-level systems (TLSs).

Below about 100 mK, the mechanical device starts to be self-driven out of equilibrium by a strong stochastic force of unknown origin. We report on this phenomenon with a detailed account of the observed features, which have been confirmed in different laboratories but never documented to our knowledge [23–25]. This thorough description is calling for theoretical understanding, and we speculate on the possible ingredients that could be underlying this effect. We demonstrate that the strongest events can be canceled by applying a dc voltage onto the transmission line. However, for beam-based devices the remaining (small) events seem to limit the measurement capabilities to about 10 mK, roughly the lowest achievable temperature for dilution cryostats. This is actually an order of magnitude better than what has been reported so far for doubly clamped beams [14,26,27]. Looking also at the spread in the reported thermalization temperatures of drumlike devices, obtained in *completely similar* conditions, we suspect that this genuine phenomenon should be present in all devices sharing the same microwave readout scheme and constitutive materials, at different levels of expression. In this respect, the present description is extremely relevant for the community, and calls for further experiments on other types of devices *below* 10 mK.

By carefully characterizing the self-heating due to the *continuously* injected microwave power, we infer that for the extremely weakly coupled mode used here the technique is suitable down to temperatures of the order of 1–2 mK; for much larger couplings (like in drum structures) where less power is needed, in the *absence* of any uncontrolled intrinsic drive the technique should be functional down to the lowest achievable temperatures. As a comparison, similar experiments in the millikelvin range using optics could only be performed in pulsed mode [28].

II. EXPERIMENT

The microwave setup that we choose for this demonstration is relatively basic, and resembles the one described in Ref. [5]. Details on the microwave wiring can be found in Appendix A. The measurement is performed in transmission, with a coplanar transmission line coupled on chip to microfabricated microwave cavities (see Fig. 1 left). The practical aspect of this design is multiplexing: in Fig. 1 one cavity hosts our on-chip thermometer while the others can be used for more complex experiments.

The microwave cavities are realized through laser lithography and reactive ion etching (RIE) of a 120-nm-thick layer of niobium (Nb). A typical resonance curve at about $\omega_c/(2\pi) \approx 6$ GHz is shown in Fig. 1 center, displaying a (bidirectional) coupling rate of $\kappa_{\mathrm{ext}}/(2\pi) \approx 100$ kHz and a total damping rate of about $\kappa_{\mathrm{tot}}/(2\pi) \approx 150$ kHz. The NEMS mechanical element we use as an on-chip thermometer is made from 80-nm-thick high-stress silicon nitride (SiN, 0.9 GPa), grown on top of silicon. It is a 50-μm-long doubly clamped beam of width 300 nm. It is covered by a 30-nm layer of aluminum (Al), capacitively coupled to the cavity through a 100-nm gap. The aluminum part is patterned using standard e-beam lithography and lift off, while the beam is released through RIE etching of the silicon nitride followed by a selective XeF$_2$ silicon etching [29]. The silicon nitride is not removed below the niobium layer. The mechanical resonance of the first flexural mode we use is shown in Fig. 1 right, around $\Omega_m/(2\pi) \approx 4$ MHz, with damping rate $\gamma_m/(2\pi)$ of order 10 Hz. Such a mechanical mode still hosts about $n_{\mathrm{thermal}} \approx 6$ phonons around 1 mK, large enough to be considered in the *classical* limit and thus well adapted to mode thermometry.

The microwave setup is carefully calibrated by electronic means; we therefore quote injected powers in Watts applied on chip, and detected spectra in W/Hz (expressed in the *number of 6 GHz photons*) at the output port of the chip. These units are adapted to both issues of heat leaks (cryogenics) and signal to noise (electonics) discussed in this Paper. Two setups are used: a dry commercial BlueFors® (BF) machine for preliminary experiments (base temperature 7.5 mK), and then the homemade Grenoble nuclear adiabatic demagnetization cryostat
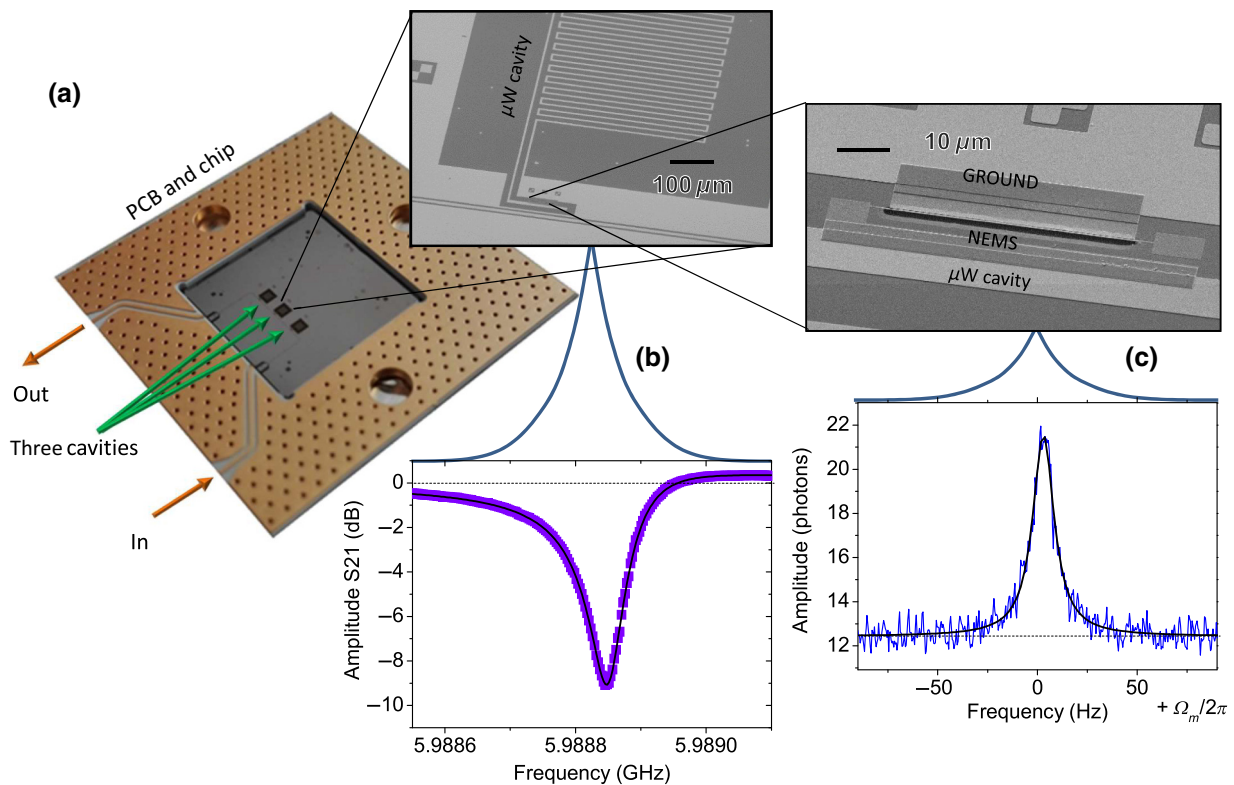
FIG. 1.   Chip arrangement. (a) Chip before bonding in a microwave printed circuit board (PCB), displaying a coplanar transmission line coupled to three microwave cavities. (b) Cavity and resonance [data violet squares, black line is a fit to Eq. (B1)] at 210 mK with blue-detuned pump power 7 nW and probe power 25 fW. (c) NEMS beam structure and resonance spectrum measured on the Stokes peak for blue-detuned pump power 0.5 nW at the same temperature (negligible optomechanical back action, data blue line, and black line is a Lorentzian fit with $\Omega_m \approx 2\pi \times 3.79$ MHz, see Appendix B for details).

(operated down to 400 μK) [30]. Particular care is taken in the construction of the two cryostats' temperature scales, and details are given in Appendix A.

The optomechanical interaction arises from the force exerted by light onto movable objects [19]. It corresponds to the transfer of momentum carried by light (i.e., photon particles) to the surfaces on which it reflects. In a cavity design with one movable mirror, the retarded nature of this so-called radiation pressure force (due to the finite lifetime of light inside the cavity) leads to damping or antidamping of the motion, depending on the frequency detuning of the input light with respect to the cavity [19].

Our moving end mirror is the NEMS beam capacitively coupled to the microwave resonator of Fig. 1 (the cavity) [5]. The standard schemes we use are illustrated in Fig. 2, with an input wave of power P_{in} at frequency $\omega_c + \Delta$. We are in the so-called resolved-sideband regime, with $\gamma_m, \kappa_{tot} \ll \Omega_m$ [19]. When we pump power in the system exactly at the frequency of the cavity ω_c (detuning $\Delta = 0$), the mechanical motion leads to a phase shift of the light [19]. The Brownian motion of the mechanical element thus imprints two equivalent sidebands in the spectrum that we can measure. For a red-detuned pump (frequency detuning

$\Delta = -\Omega_m$, Fig. 2), energy quanta from the mechanics (phonons) can be transferred to the optical field (photons). This leads to the well-known sideband-cooling technique [19,31,32]. The so-called anti-Stokes sideband peak in the spectrum is favored, and the mechanical mode is *damped* by light. On the other hand, for a blue-detuned pump ($\Delta = +\Omega_m$, Fig. 2), the optical field generates a parametric instability in the mechanics [19,33]. The Stokes sideband peak is favored, and the mechanics is amplified through *antidamping*. Eventually one can reach at high pumping powers the self-oscillation regime [34,35].

We start by calibrating the optomechanical interaction. The optical damping and antidamping are linear in applied power P_{in}, see Fig. 3. From a fit [Eq. (3) below], we can infer the so-called single-photon coupling strength $g_0 = \frac{1}{2}\omega_c(1/C)(dC/dx)x_{zpf}$ with x_{zpf} the zero-point-motion [19]. This is essentially a *geometrical* parameter, arising from the modulation dC/dx of the microwave mode capacitance C by the beam motion [5]. We find $g_0/(2\pi) \approx 0.55 \pm 0.1$ Hz, corresponding to the out-of-plane flexure. This coupling is particularly small, the idea being to take advantage of that to demonstrate the sensitivity of our method. The magnitude of the output
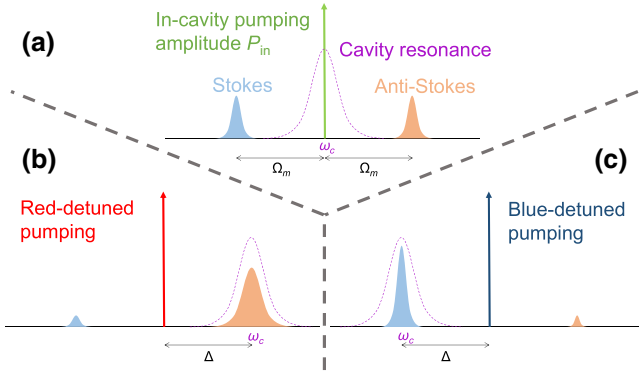
FIG. 2. Optomechanical schemes used (drawing not to scale, frequency domain). (a) "In-cavity" pumping, a strong tone (in green) is applied at the cavity resonance and the two (equivalent) sidebands are measured. (b) Red-detuned pumping: a strong microwave signal is applied (in red) at a frequency detuned from the cavity ω_c by $\Delta = -\Omega_m$, and we measure the so-called anti-Stokes peak at ω_c. (c) Blue-detuned pumping: a strong pump tone (in blue) is applied at frequency $\omega_c + \Omega_m$, while we measure the Stokes peak.

power is fit to theory [19], leading to a calibration of the measured phonon-mode population and temperature [performed at 210 mK, parameter $\mathcal{M}$ in Eq. (1) and Fig. 14]. More details on the optomechanics measurements can be found in Appendix B.

III. METHOD

The method we propose builds on the parametric instability of the blue-detuned pumping scheme. When the pump tone is applied at ω_c, the size of the two equivalent
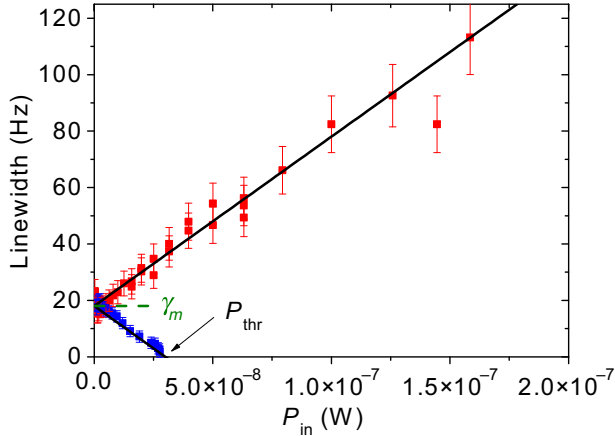

FIG. 3. Effective damping and antidamping γ_{eff} measured for the blue- and red-detuned pumping schemes as a function of power (at 210 mK, blue and red squares, respectively). The slope of the fit (black line) leads to the definition of g_0, while $P_{\text{in}} \approx 0$ corresponds to γ_m. The arrow indicates the position of the threshold P_{thr} towards self-sustained oscillations, which is simply proportional to γ_m (see text).

sideband peaks (their measured area $\mathcal{A}_0$, in photons/s) is simply proportional to injected power P_{in} and mode temperature T_{mode} [19]:

$$\mathcal{A}_0 = \mathcal{M} P_{\text{in}} T_{\text{mode}}. \tag{1}$$

This optomechanics scheme alters neither the measured position of the sideband peaks (detuned by $\pm\Omega_m[T_{\text{beam}}]$), nor their linewidth $\gamma_m(T_{\text{beam}})$: both are determined by mechanical properties, which depend on the beam temperature T_{beam}. The lineshapes are Lorentzian. We introduce the *number of stored photons* in the cavity n_{cav}, function of both P_{in} and Δ:

$$n_{\text{cav}}(P_{\text{in}}) = \frac{P_{\text{in}} \kappa_{\text{ext}}/2}{\hbar(\omega_c + \Delta)(\Delta^2 + \kappa_{\text{tot}}^2/4)}. \tag{2}$$

On the other hand, for blue-detuned pumping, as we increase the injected power P_{in} (but keep it below the instability threshold), the area $\mathcal{A}$ of the Stokes peak is amplified. The blue- and red-detuned pumping expressions write [19]

$$\gamma_{\text{eff}}(P_{\text{in}}) = \gamma_m - \text{Sign}(\Delta)\frac{4g_0^2 \, n_{\text{cav}}(P_{\text{in}})}{\kappa_{\text{tot}}}, \tag{3}$$

$$\mathcal{A} = \mathcal{A}_0 \times \frac{\gamma_m}{\gamma_{\text{eff}}(P_{\text{in}})}, \tag{4}$$

in the limit of negligible cavity thermal population. For $\Delta > 0$, the last term in Eq. (4) after the $\times$ sign is a gain, illustrated in Fig. 4. It arises from the antidamping, with
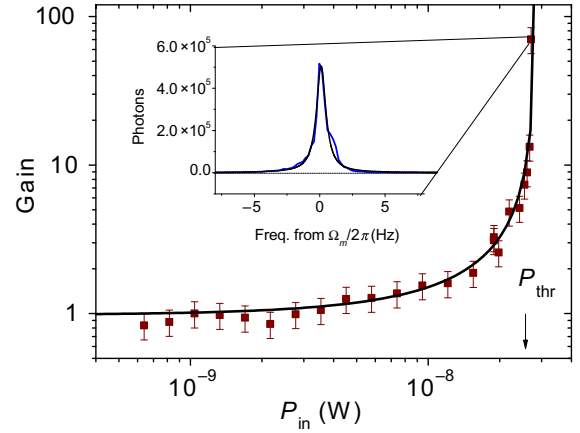

FIG. 4. Main: gain of the parametric amplification method based on the blue-detuned pumping scheme (210 mK data, brown squares), as a function of P_{in}. As in Fig. 3, the arrow indicates the position of the threshold P_{thr} towards self-sustained oscillations. Inset: resonance line (blue trace) measured at very large gains, demonstrating its Lorentzian lineshape (linewidth of order 0.9 Hz, close to instability). The black lines are fits, and we report about 20-dB amplification of the Brownian signal. Finite error from both statistics and fluctuations in mechanical parameters (see text).
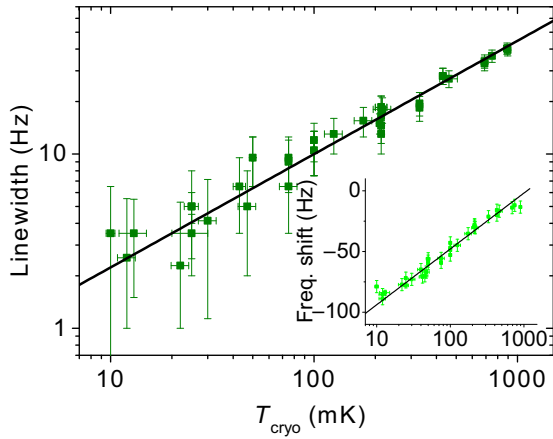
FIG. 5. Main: mechanical damping parameter γ_m as a function of cryostat temperature T_{cryo}. Inset: resonance frequency shift from $\Omega_m(T^*)$ of the flexural mode in the same conditions. Black lines are fits following the TLS model ($\alpha \approx 0.65$, $T^* \approx 1.1$ K see text). Note the scatter in the data (also in Fig. 3), further discussed in Sec. V.

γ_{eff} the linewidth of the Lorentzian peak. Controlling the applied power P_{in}, from the knowledge of system parameters one can straightforwardly recalculate the value of $\mathcal{A}_0$, and thus of T_{mode} (i.e., the temperature of the mode *in absence of* optomechanical pumping). In Fig. 4, we demonstrate 18.5-dB gain, which is greater than the previously reported maximum for a similar setup using a graphene device [35]. Essentially *only* γ_m depends on temperature, and has to be known to apply Eq. (4). It can be obtained easily from a measurement of the mechanical effective damping (the linewidth of the Lorentzian Stokes peak, Fig. 3), by either extrapolating to $P_{\text{in}} \to 0$ or defining the position of the threshold $P_{\text{thr}} \propto \gamma_m$ [with Eq. (3) at $\gamma_{\text{eff}} = 0$, see Figs. 3, 4, and 15]. More details are given in Appendix B. Obviously, the main requirement for this T_{mode} estimate is the *stability* of experimental parameters. The mechanical mode itself happens to be the limiting element (see Figs. 3 and 5 below), leading to finite error bars at large gains in Fig. 4; fluctuations are further discussed in Secs. IV and V, see Fig. 8.

The measured mechanical damping rates γ_m and resonance frequencies Ω_m are shown in Fig. 5. The displayed dependencies are characteristic of NEMS devices in the millikelvin range: a damping $\gamma_m \propto T^\alpha$ with $0.3 < \alpha < 2.5$ and a logarithmic frequency shift $\propto \ln(T/T^*)$ with T^* a characteristic temperature (see fits in Fig. 5). For all materials (from monocrystalline to amorphous) this behavior is understood as a signature of TLSs [28,36–41]: either defects (e.g., for monocrystalline Si, or polycrystalline Al), or constitutive of the atomic arrangement (for amorphous SiN). Direct coupling of the first flexural mode to the phonon bath (i.e., clamping losses) [42] is negligible for these structures at millikelvin temperatures.

Within the TLS model the mechanical mode is coupled to the two-level systems, which are themselves coupled to the external bath: the electrons and the (thermal) phonons present in the moving structure [39]. For superconducting materials, the electronic contribution is negligible and the temperature of the TLSs should reflect the phononic temperature in the beam (i.e., the temperature of high-frequency modes well coupled to the clamping ends), which we simply define as T_{beam}. By inverting the fits in Fig. 5 it is thus straightforward to extract T_{beam}.

The aim of our work is thus to compare the temperature of the cryostat T_{cryo} to T_{beam} and T_{mode}. These results are analyzed in Sec. IV; however it is mandatory to quantify beforehand the impact of the microwave pump power on the defined temperatures. For this purpose, we use the "in-cavity" pumping scheme (Fig. 2). We measure, at a given temperature T_{cryo}, the mechanical characteristics γ_m, Ω_m, and the area $\mathcal{A}_0$ of the two sideband peaks as a function of injected microwave power P_{in}. Using, respectively, the fits of Fig. 5 and Eq. (1), we can recalculate the expected temperatures T_{beam} and T_{mode} under microwave irradiation. Since the local heating should be proportional to the local electric field squared confined onto the NEMS, we discuss these results as a function of n_{cav}. The properties of the cavity itself as a function of the pump settings are discussed in Appendix B.

A typical result obtained at 210 mK is shown in Fig. 6 (main graph). Both T_{beam} (obtained equivalently from damping and frequency shift) and T_{mode} display *the same* linear dependence on n_{cav}, and the two sidebands are equivalent: this demonstrates that the effect is indeed thermal. Defining the slope of the fit as σ, we can extract this coefficient as a function of T_{cryo} (Fig. 6
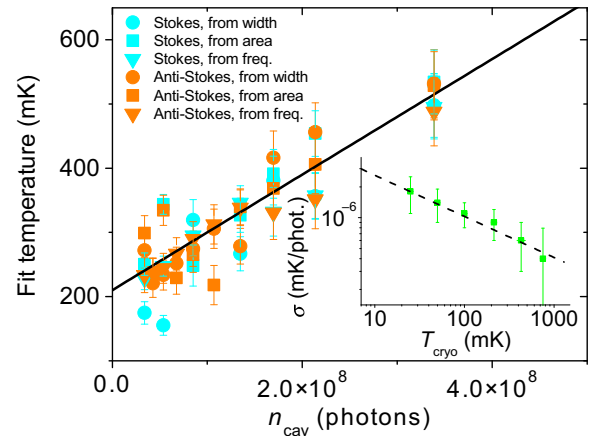

FIG. 6. Main: microwave heating as a function of n_{cav} performed at 210 mK, with temperatures recalculated from the measured width and position (corresponding to T_{beam}) and peak area (T_{mode}). The line is a linear fit, leading to the microwave-heating coefficient σ. Inset: heating coefficient σ versus cryostat temperature T_{cryo}; the dashed line is a power law guide to the eye.

inset). This temperature dependence is nontrivial, and no heating model is provided here: such a model should take into account the microwave absorption in the materials, the energy flow in the beam *plus* the clamping zone slab (suspended by the fabrication undercut), and finally the anchoring to the bulk of the chip. Nonetheless, we can use this graph to estimate the NEMS heating for a given T_{cryo} and n_{cav} in the blue-detuned pumped scheme. As a result, we extrapolate that applying a power of order P_{thr} at 1 mK would heat the beam by about 1 mK; above 10 mK, the heating is essentially negligible (see error bars on the T axis of Fig. 15). Knowing the smallness of the coupling g_0 employed here, this demonstrates the capabilities of the method. Furthermore, because of this microwave heating it is obviously meaningless to report experiments below about $T_{cryo} \approx 1$ mK for this first "ultimate" cooling attempt.

IV. IN-EQUILIBRIUM RESULTS

From fits to Eq. (4) of the power-dependent Stokes peak area, we thus extract T_{mode}. Reversing the fits of the mechanical parameters γ_m, Ω_m (Fig. 5) we obtain T_{beam}. Both are displayed as a function of T_{cryo} in Fig. 7, for our two experimental setups. We demonstrate a thermalization from about 10 mK to 1 K of the mode and of the whole beam; the device *is in thermal equilibrium* over 2 orders of magnitude in T_{cryo}. The reported lowest thermodynamic temperatures in the literature lie all within the range 10–30 mK [2–5,10–13,32,35]; however one work reports a potential mode temperature for an Al drum of order 7 mK, consistent with the base temperature of dry-dilution cryostats [43]. Similarly, a lowest temperature of 7 mK is reported for a gigahertz phononic crystal [41]; but obviously such a mode cannot be used for phonon thermometry at millikelvin temperatures.

As far as thermalization between *measured* T_{cryo} and T_{mode}, T_{beam} is concerned, Fig. 7 reproduces the state of the art, but does not go yet beyond even though the cryostat cools well below 7 mK. The reason for this is discussed in Sec. V: below typically 100 mK, the system displays *huge amplitude fluctuations*, which hinder the measurements (Fig. 8). These features have been seen by other groups for *beam-based microwave optomechanical devices containing an aluminum layer*, but never reported so far [23–25,44]. Until recently, this essentially prevented experiments from being performed on these types of devices below physical temperatures of order 100 mK [14,26,27]; remarkably however, (Al-covered) ladder-type Si beams [11,44] seem to be less susceptible to this problem than simple doubly clamped beams. On the other hand, large signal fluctuations *have not* been observed to date for (Al) drumlike structures [23,25], and do not show up in schemes, which *do not* involve microwaves (e.g., magnetomotive measurements of SiN and Al beams [37,45], or
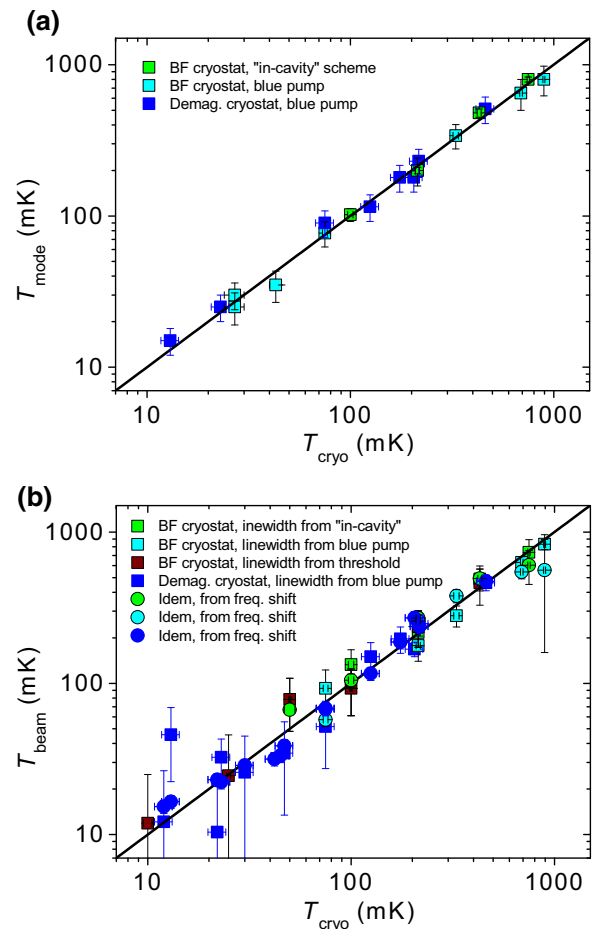

FIG. 7. (a) Mode temperature T_{mode} as a function of cryostat temperature T_{cryo}. (b) Beam temperature T_{beam} inferred from the TLS bath as a function of T_{cryo}. The conditions of the measurements are defined in the legend. The line is the $y = x$ function.

laser-based measurements of Si beams [28]). This is what enabled nanomechanical experiments to be conducted at base temperature of dilution cryostats.

Up to now, the only possibility to deal with these large events was *postselection*, which is extremely time consuming and even stops being useable at all at the lowest temperatures. The origin of this phenomenon remains unknown, and we can only speculate on it in Sec. V hereafter. Note that there is *no evidence* of thermal decoupling in Fig. 7.

More conventional frequency Ω_m and damping γ_m fluctuations [46] are also present (see, e.g., Fig. 8). These features have been reported for essentially all micro and nanomechanical devices, as soon as they were looked for; their nature also remains unexplained, and their experimental magnitude is much greater than all theoretical expectations [47]. Frequency noise essentially leads to inhomogeneous broadening [48]. It *does not* alter the area $\mathcal{A}$ measurement, but does corrupt both frequency and
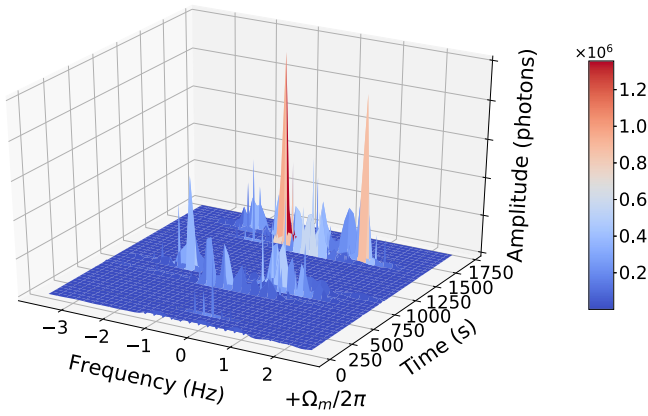
FIG. 8. Stokes resonance peak (amplitude in color scale, frequency from Ω_m on the left) as a function of time at about 1 mK (0.6 nW applied power, blue-detuned pumping scheme). Huge amplitude jumps are seen, together with frequency (and damping) fluctuations (see text).

linewidth estimates. This noise comes in with a $1/f$-type component [46,47], plus *telegraphlike jumps* [49]. It leads to the finite error bars in Fig. 5 inset; below 10 mK, the mechanical parameters Ω_m and γ_m cannot be measured accurately. Similar damping fluctuations [46] are more problematic, since the amplification gain Eq. (4) depends on γ_m. The error bars of Fig. 5 (main graph) are essentially due to this; they translate into a finite error for the estimate of the gain, Fig. 4, which itself limits the resolution on T_{mode} (Fig. 7, top).

V. UNSTABLE DRIVE FORCE FEATURES

In Fig. 8 we show a typical series of spectral acquisitions as a function of time, around 1 mK. We see very large amplitude fluctuations, which start to appear around 100 mK, and get worse for lower temperatures (regardless of the scheme used): the "spikes" grow even larger, but more importantly *their occurrence* increases. We study these events in the whole temperature range accessible to our experiment. Their statistics seem to be rather complex, and shall be the subject of another Paper. Key features are summarized in this section. For blue-detuned pumping, the spikes worsen as pump power increases, while for red-detuned pumping it is the opposite, suggesting that the effective damping of the mode plays an important role. With in-cavity pumping, spiky features are also present at very low powers, but not at high powers when the NEMS physical temperature exceeds about 100 mK. The recorded heights can be as large as equivalent mode temperatures in the Kelvin range. Around 10–30 mK, postselection becomes impossible.

With the aim of searching for the origin of this effect, we characterize it in various situations. We first realize that cycling the system from the lowest temperatures to above
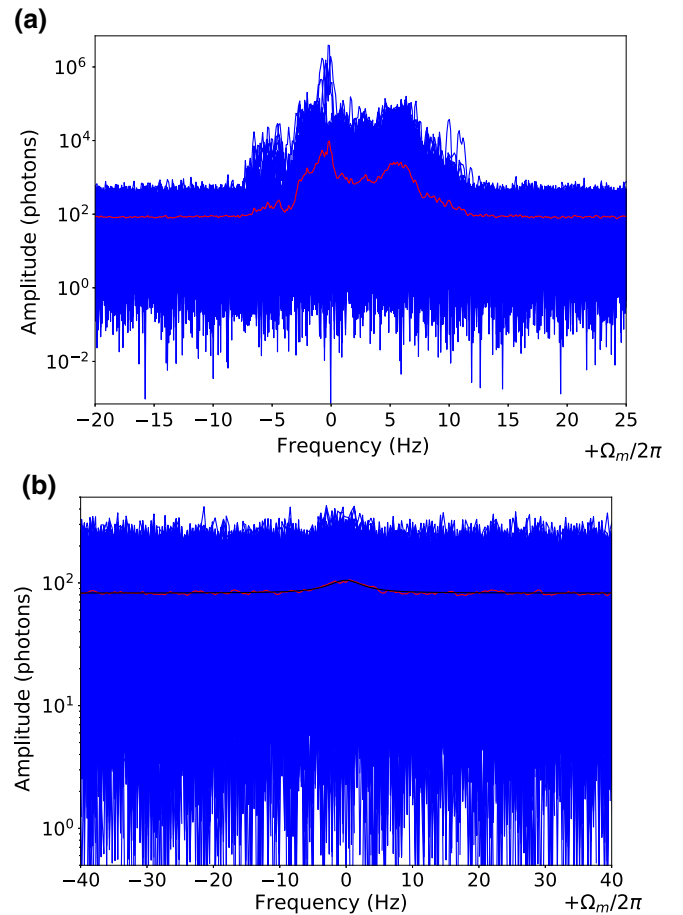
(a)

(b)

FIG. 9. Comparing measurements with and without applied dc voltage in similar conditions. (a) Resonance lines (blue) obtained at 5 mK with 0.6-nW drive; 2-h acquisition shown in 560 averaged traces, with *no* dc voltage bias. (b) Resonance lines obtained at 7 mK with 0.8-nW drive; 18 h in 770 averaged traces, with $+3$ V dc applied on the transmission line (see text). The scheme used for both data sets is blue-detuned pumping, and the thick black line is a fit of the average curve (in red). Note the 10^4 difference in the vertical axes.

100 mK is producing a sort of "reset." But very quickly (a matter of hours), after cooling down again the large spikes happen to dominate the signal again. We then try to apply a small magnetic field to the system; this was not very conclusive. However, applying a dc voltage has a drastic effect on these random features. This is illustrated in Fig. 9: with a few volts on the chip's coplanar transmission line *all the large features disappear*. The averaged signal (deeply buried into the noise) recovers a reasonable Lorentzian lineshape (see fit in Fig. 9), while the shape of the spikes is not resolved (Fig. 8). Details on the dc voltage biasing are given in Appendices A and B.

In discussing the source of this feature, a few comments have to be made. What is shown in Fig. 8 is primarily fluctuations of the *output* optical field. These are detected *only* on the Stokes and anti-Stokes peaks, for any of the

schemes shown in Fig. 2. Furthermore, the threshold to self-oscillation in the blue-detuned pumping scheme displays a large hysteresis (certainly due to nonlinearities in the system, see Fig. 15, Appendix B). We notice that when the microwave power applied (at frequency $\omega_c + \Omega_m$) lies within this hysteresis, the spiky events seem to be able to trigger the self-oscillation. This is not possible if the amplitude fluctuations measured are only in the detected signal, at the level of the high electron mobility transistor (HEMT). We thus conclude that we see genuine *mechanical* amplitude fluctuations. However, these cannot be due to damping fluctuations alone that could trigger self-oscillations, since we do see the same types of features when performing red-detuned or in-cavity pumping.

If these fluctuations are due to the input field itself, from Fig. 6 we can reasonably conclude that the NEMS beam is heated to rather high temperatures, leading to broad and very shifted in frequency (see Fig. 5) Stokes and anti-Stokes peaks. This is not compatible with the measurement of Fig. 8. The only reasonable conclusion seems thus to be that we do suffer from a *genuine extra stochastic force* acting on the mechanical element. This is consistent with a stronger sensitivity to the phenomenon when the effective damping of the mode is small (blue-detuned scheme). Since a dc voltage applied *only to the cell* can drastically modify the measured features, the source has to be on chip. Noting, furthermore, that with an in-cavity pumping, it disappears when the beam temperature exceeds 100 mK, we conclude that it *should even be within the mechanical element*. But the mechanism remains mysterious: citing only documented effects in other areas of research, is it linked to vortex motion in the superconductor [50], trapped charges [51], adsorbed molecules [52] or to atomic-size two-level systems in dielectrics (beyond the standard friction model) [53]?

The low-temperature properties of NEMS are described within the tunneling model of TLSs for damping, frequency shifts, and phase fluctuations [28,46,54]. It is thus natural to consider strongly coupled individual TLSs as the most probable source of our problems. Besides, while the actual nature of these microscopic defects remains elusive in most systems, they could be generated in many ways beyond the standard atomic configuration argument [55]; an electron tunneling between nearby traps is a TLS strongly coupled to its electromagnetic environment, among other possibilities [52]. For Al-based NEMS, these would create (only a few) defects present in (or *on*) the Al layer; they should carry a dipole moment, which couples them to the microwave drive as well as to the electric field generated by the applied dc voltage. This field distorts their potentials, such that they could get locked in one state and "freeze." Furthermore, our results seem to be very similar to those of Ref. [56] obtained with a *macroscopic* mechanical glass sample, where "spiky" events were demonstrated to be originating in the interaction

with low-level radioactivity (gamma rays). These results suggest a parametric coupling to the TLS at gigahertz frequencies mediated by the microwave drive, but where the energy corresponding to the large peaks is provided by the external radiation.

The reason why the mechanism should be dependent on the low phononic dimensionality or size of the device (typical width about 100 nm, much smaller than the phonon wavelength at 10 mK) is nontrivial. One simple argument can be that the spring constant of the modes under consideration are very different: about 1 N/m for megahertz beams and 100 N/m for drumheads. This can justify why beam-based structures are more reactive to external force fluctuations; an immediate consequence of this argument is then that membrane-based Al devices *are not* truly immune to force fluctuations, but are just less sensitive: if that should be true, cooling them to low enough temperatures would eventually revive the same features as for beam-based NEMS.

To conclude, let us concentrate on the measurements performed at ultra-low temperatures with a dc voltage bias (of the type of Fig. 9, bottom). Even with the help of the in-built parametric amplification, the signal is very small and requires decent averaging, typically here about 30 min for reasonable error bars. Even if the resonance peak is Lorentzian, below typically 20 mK the measured area $\mathcal{A}$ does not correspond to the actual cryostat's temperature T_{cryo}: it is always bigger, but the actual value presents *large fluctuations* in magnitude. This is demonstrated in Fig. 10,
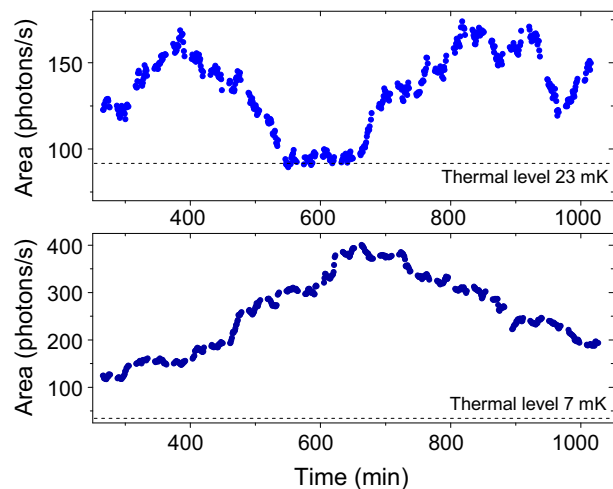

FIG. 10. (a) Area of peak extracted from a sliding average performed with a window of 26 min at 23 mK, with applied power 0.8 nW (blue-detuned pumping). (b) Same measurement performed at 7 mK. The horizontal dashed lines are the thermal population expected values, matched at 23 mK in the stable zone (middle of graph). At the lowest temperatures, we observe very large amplitude fluctuations, which *cannot be* of thermal origin; the measured area remains always larger than the expected value (see text).

with identical measurements performed at 23 and 7 mK. What is shown is how the measured area of the Stokes peak evolves over time, performing a sliding average over the whole set of acquired data. In the former case, we see that the fluctuations of the measured area are not more than about +60%; they are much smaller for higher temperatures, leading to proper estimates of T_{mode}. However, for the latter these are greater than 300%. Besides, fluctuations happen to have an extremely slow dynamics: while spikes switch on and off faster than our acquisition time, their overall occurrence fluctuates over *a day* (Fig. 10). By no means can this behavior be explained by a thermal decoupling of the device from the cryostat. As a consequence, even the calm zones in Fig. 8 are corrupted by the phenomenon shown in Fig. 10. This is essentially why no reliable data can be acquired below 10 mK; but from the dc biasing and the continuous monitoring of the Stokes peak, thermal equilibrium is demonstrated at about ten times lower temperature than previously reported in microwave doubly clamped NEMS experiments [14,26,27].

VI. CONCLUSION

We present measurements of a microwave optomechanical system performed on a nuclear adiabatic demagnetization cryostat, able to reach temperatures well below the 10 mK limit of conventional dilution machines. Relying on a fairly standard microwave wiring and the in-built parametric amplification provided by a blue-detuned pumping, we devise a method providing accurate thermometry of both the mechanical mode and its on-chip environment (the two-level systems to which it couples). The experiment is conducted on a beam nanoelectromechanical system embedded in an on-chip microwave cavity. The efficiency of the method is demonstrated with a very low optomechanical coupling. Thermalization is shown from 10 mK to 1 K with no sign of thermal decoupling.

However, at very low temperatures we report strong fluctuations in the signal amplitude, which prevented any experiments being conducted at ultra-low temperatures. These features appear around 100 mK and have been observed in different laboratories, but had never been studied in details so far. We demonstrate the characteristics of these fluctuations, and argue that they are due to an extra stochastic driving force of unknown origin. Microwave irradiation seems to trigger the phenomenon. Applying a dc voltage of a few volts on chip cancels the large spiky events, but a small component of this extra random drive persists, with variations over a typical timescale of about a day.

It is unclear if all the fluctuation characteristics present in the devices (amplitude, frequency, damping) are linked to the same underlying mechanism. One can even imagine that temperature-dependent nonlinear effects can impact the phonon-photon coupling, beyond the lowest

(geometrical) order g_0. However, it is likely that these effects are present in *all* experimental systems at different levels of expressions, since all NEMS and MEMS share the same overall characteristics (especially damping, frequency shifts, and phase noise typical of two-level-system physics). It is thus tempting to relate this stochastic force to a mechanism mediated by some kind of microscopic TLSs, driven by microwaves but blocked under dc voltage biasing. This stochastic driving force can mimic, to some extent, a thermal decoupling, and can explain why some drumhead devices in the literature refuse to cool down below typically 20–30 mK. While being a limitation for experimentalists, this phenomenon definitely deserves theoretical investigations. The present work also calls for further experiments at lower temperatures, using other types of devices (e.g., drums). This shall be performed in the framework of the European Microkelvin Platform [57].

Note added.—Recently, a collaboration between Aalto University and Institut Néel has started with the aim of cooling down a drumhead Al device as low as possible on our adiabatic nuclear demagnetization platform. We have evidence that the same features as for beams are present, at a different level of expression. This shall be published elsewhere.

APPENDIX A: SETUP

Two similar microwave setups are used in these experiments. Their common features are described in Fig. 11. This wiring is basic and can also be found within the literature [5]. Essentially, they are built around a cryogenic HEMT placed at about 4 K and two circulators mounted on the mixing chamber of the dilution units. On the BlueFors® (BF) machine, the HEMT is a Low Noise Factory® 4–8 GHz bandwidth, with a measured noise of about 3 K (ten photons) at 6 GHz. On the nuclear adiabatic
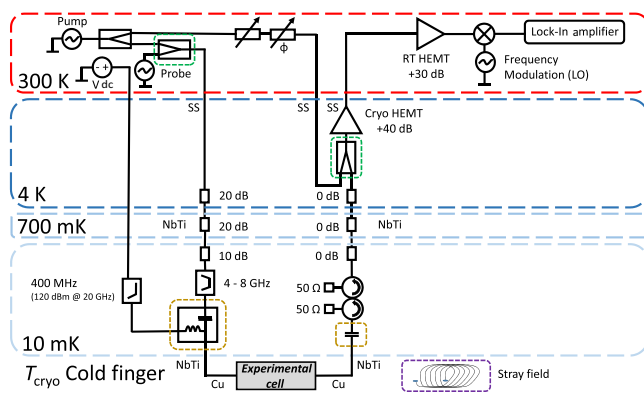
FIG. 11. Simplified common wiring of the experimental platforms; the different levels within the cryostats (BF and demagnetization) are shown with their respective temperature. SS stands for stainless steel, NbTi for niobium titanium, and Cu for Copper coaxial cables (50-ohms impedance). The boxed elements are added and removed depending on the experimental run (see text for details).

demagnetization cryostat, it is a Caltech 1–12 GHz bandwidth with a measured noise of about 15 K (50 photons at 6 GHz). The (dashed-green) boxed component below the HEMT in Fig. 11 represents a power combiner used to realize an opposition line. On the BF setup, this is mandatory to avoid saturation of the cryogenic HEMT from the strong blue-detuned pump tone. On the demagnetization cryostat, the cryogenic HEMT is linear enough so this protection is not necessary. This choice is made because of space constrains: feeding an extra microwave opposition line in the nuclear adiabatic demagnetization cryostat is very demanding. The filtering of the injection lines (dc and microwave) is also described in Fig. 11.

Gains and noise levels of the full chain are carefully checked with respect to the HEMT working point. Besides, each component is tested at 4 K prior to mounting. The whole setup is then calibrated, using an Agilent® microwave generator EXG N5173B and an Agilent® spectrum analyzer MXA N9020A. The measurements presented in the core of the paper are realized using a Zurich Instruments® UHFLI lock-in detector operating in spectrum mode. The signal is mixed down with a local oscillator (LO) and detected at frequency $\pm\Omega_m + 2$ MHz (the shift avoiding overlap of Stokes and anti-Stokes signals). The generators used are from Agilent® or Keysight® brands leading to equivalent data quality. The *absolute* error in the calibrations is estimated at about ± 2 dB over the whole set of realized runs; within these error bars, the two cryogenic platforms give the same quantitative results.

Particular care is taken in thermalization issues. The experimental cell is thus made of annealed high-purity copper. It is mounted on a cold finger either bolted onto the mixing chamber plate of the BF machine, or connected through silver wires to the bottom of the nuclear stage of

the demagnetization cryostat. This stage is of laminar type, about 1 kg of high-quality copper [30]. On the top it is connected through a Lancaster-made Al heat switch [58] to the mixing chamber of the home-made dilution unit. Both dilution cryostats reach base temperatures of order 7–10 mK depending on cooling power settings. The PCB mounted inside the cell is hollow in its center; the chip is pressed there *directly* onto the copper block, by means of a copper-indium spring. At very large microwave powers, we see heating at the intermediate stages where attenuators are anchored. However, the nuclear stage thermometers *do not* show any heating, even at the highest powers used.

Thermometry below typically 30 mK is no easy task; below 10 mK it requires the expertise of ultra-low temperature laboratories (see, e.g., EMP partners [57]). In the graphs of Fig. 7, the x axis is as important as the y axis; this point is not always emphasized in the literature. We thus pay particular care in providing an almost primary temperature scale for our two microwave platforms. The use of the word *almost* here should be understood as follows: we also use resistive thermometers (RuO$_2$, carbon Speer type) calibrated against primary devices, and our primary thermometers (which do follow known temperature dependencies) are calibrated at a single point in temperature for practical reasons. Our laboratory has a long history of working for the construction of the ultra-low temperature scale [59]. In our case, the BF cryostat is equipped with a Magnicon® MFFT noise thermometer and a cerium magnesium nitrate (CMN) paramagnetic salt thermometer. The MFFT is bolted at mixing-chamber level, while the CMN is directly mounted on the cold finger. On the demagnetization cryostat, an MFFT is mounted at the top of the nuclear stage while a ^{3}He thermometer is connected at the bottom; the experimental cell is actually *between* the nuclear stage and this thermometer. When their working range overlaps, the thermometers agree within typically 2%–5%; the error bars on x axes of the temperature plots also take into account thermal gradients and slow drifts.

The nuclear adiabatic demagnetization process requires large magnetic fields to be used (here, 8 T). One usually starts at $T_{ini} \approx 10$ mK with the superconducting coil surrounding the stage fully magnetized at B_{ini} (heat switch open), and then demagnetizes to about $B_{fin} \approx 100$ mT to reach the lowest possible temperatures (in the present runs, we work down to 400 μK, Fig. 12). The cryostat can then stay cold over a week (heat leak < 100 pW); another cycle needs then to be initiated with a precooling of the system. The process being adiabatic, the nuclear spins of copper are cooled according to $B_{ini}/B_{fin} = T_{ini}/T_{fin}$ [60]. Our magnet is compensated on both sides, but nonetheless small stray fields are present when it is magnetized (represented in Fig. 11 by the small boxed coil). In order to make sure that these fields do not introduce any slant in the data, we perform measurements *above* 10 mK but within a demagnetization cycle: we start at 20 mK instead
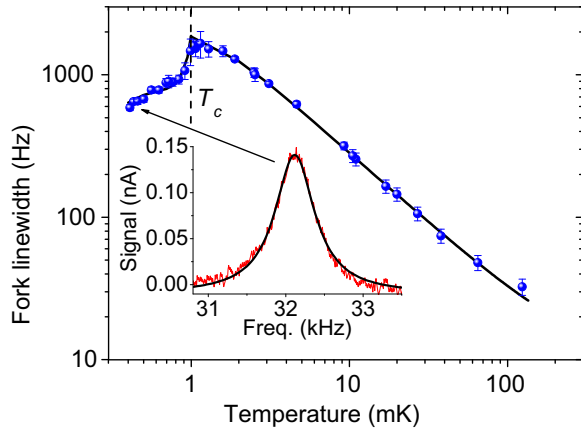
FIG. 12. Calibration measurements performed on the ^{3}He thermometer, from the lowest operated temperature (here 400 μK, raw data fork resonance curve in the inset with Lorentzian fit) to about 100 mK. The superfluid transition T_c is clearly visible around 1 mK and can be used as a temperature fixed point; the line is the expected behavior from ^{3}He viscosity, see text.

of 10 mK, and reduce the field by 1/2. This can then be compared to experiments performed without any field, at base temperature of the dilution unit. The microwave cavity shifts in frequency with applied field (see Appendix B), but no other difference can be found. All data taken below 10 mK are obtained exclusively with the nuclear adiabatic demagnetization technique.

The lowest part of our temperature scale is obtained from a ^{3}He thermometer (see Fig. 12). It is based on the viscosity measured in the fluid with an immersed probe, a mechanical resonator. In the past, vibrating wires were the best choice for this task [61,62]. Today, people use quartz tuning forks, which are more practical [21,63,64]. Our thermometer is thus a nested cell containing two tuning forks (one in the outside cell, the other in the inside), filled with silver sinters connected to the nuclear stage by silver wires. The outside cell serves as a thermal shield for the inner one, and does not cool down below typically 1 mK. The inner cell is directly connected to the cold finger that hosts the microwave cell.

^{3}He is a Fermi liquid above about 1 mK, and becomes superfluid below. At 0-bar pressure, 0-T field this state is called ^{3}He-B, and the properties of this amazing fluid have been extensively studied over the years [65]. For instance, the viscosity of ^{3}He is well known for both normal and superfluid states, see, e.g., [66,67]. In principle, from the knowledge of the geometry of the immersed object and its surface rugosity, one can calculate the friction and thus the broadening of the resonance. In practice, it is much more efficient to calibrate the device by scaling its properties on known measurements [63,64].

In order to perform this scaling, we measure the damping of the quartz tuning-fork thermometer (inner cell) as a function of the final field of the demagnetization process

B_{fin}. The protocol is to demagnetize by steps, and then remagnetize to B_{ini} in order to verify that the process is indeed adiabatic (by recovering the initial temperature T_{ini}). It is then straightforward to calculate the temperature of the nuclear spins of copper for each step, which should be in equilibrium with electrons (and finally ^{3}He) if one waits long enough. The result is shown in Fig. 12. The line is the expected behavior from published results. Note that the superfluid transition T_c also acts as a *fixed point* in the temperature scale.

APPENDIX B: MICROWAVE OPTOMECHANICS

The microwave cavity is the central element of the technique. It happens to be very sensitive to external conditions: cell temperature, pump settings (power, detuning), dc voltage bias, and magnetic field. In order to avoid any systematic error, the protocol is thus to measure the cavity *for each setting*. On the BF cryostat, in order to mimic stray fields from the demagnetization protocol and to study the impact of (small) magnetic fields on the unstable features reported in Sec. V, a small coil is installed on top of the cell (boxed element in Fig. 11). It can create perpendicular fields up to about 10 μT. The voltage dc bias is applied *only* to the cell, which is placed within a bias tee and a dc block (see boxed elements in Fig. 11). Above about 4 V, the chip starts to heat (certainly because of currents flowing within the silicon). All reported measurements obtained with a dc bias are thus acquired at 3-V dc, ramping slowly periodically (every 1/2 h, approximately) the voltage to almost 4 V and back again. At zero bias, after some time the "spikes" eventually reappear. They do not seem to react particularly to the small magnetic fields used.

The cavity parameters are extracted from a transmission response measurement (amplitude of S_{21} component of $[S]$ matrix). This is measured by applying a very weak probe tone (see boxed element in Fig. 11) while keeping the strong pump on. We verify that the probe power is small enough not to alter the measurement. The data (see Fig. 1) is fit to the expression [68]:

$$(S_{12}[\omega])_{dB} = 20 \log \left| 1 - \frac{Q_{\text{tot}}(Q_{\text{ext}} + IQ_{\text{im}})^{-1}}{1 + 2IQ_{\text{tot}}\frac{\omega - \omega_c}{\omega_c}} \right|, \quad \text{(B1)}$$

with I the pure imaginary, $Q_{\text{tot}} = \omega_c/\kappa_{\text{tot}}$ and $Q_{\text{ext}} = \omega_c/\kappa_{\text{ext}}$. Q_{im} corresponds to an imaginary component of the external impedance, usually attributed to the inductive bonding wires (leading to the asymmetry of the fit in Fig. 1 center).

The fits are always of good quality. κ_{ext} is very stable and reproducible, and does not vary by more than about $\pm 5\%$. On the other hand, $\kappa_{\text{tot}} = \kappa_{\text{ext}} + \kappa_{\text{in}}$ varies between typically 120 and 190 kHz from one cool down to the other. κ_{in} represents the internal decay processes, taking

into account all microscopic mechanisms. At low pump powers, $\kappa_{\rm tot}$ happens to be worse (i.e., larger) than at high powers. This is true up to some maximum above which we start to substantially degrade the cavity's properties; in terms of $n_{\rm cav}$ this limit lies in the range of $10^8 - 10^9$ photons. In the range studied the temperature dependence of $\kappa_{\rm tot}$ is rather small. It is immune to the magnetic fields and voltages applied within the parameter range studied. However, the *resonance position* of the cavity is very sensitive to all parameters: so the main issue of the fit is to define ω_c as accurately as possible.

The properties of the cavity are too complex to allow an analysis of the type of Fig. 6 (performed for the NEMS), which can tell us by how much the microwave mode (and/or the chip) heats at a given pump power. We therefore measure directly the thermal population of the cavity with respect to $P_{\rm in}$. We present these data in Fig. 13 as a function of $\sqrt{n_{\rm cav}}$: on pure phenomenological grounds, the dependence seems then to be linear (see guides for the eyes in Fig. 13). We can not perform this measurement below typically 400 mK because the signal is too weak. The power dependence is rather different from Fig. 6 and does not seem to be a true heating of the chip itself; it has thus to be noise fed into the cavity by the pump generator. Indeed, similar features but with different levels of cavity populations are measured using different brands of generators. The relevant outcome of this graph is the *extra (out-of-equilibrium) cavity population* induced by the strong pump; this is the number quoted in magenta in Fig. 13 for each temperature, at the largest powers displayed. This number is obtained by dividing the photon flux by $\kappa_{\rm ext}/2$ (bidirectional coupling). Injecting it in the
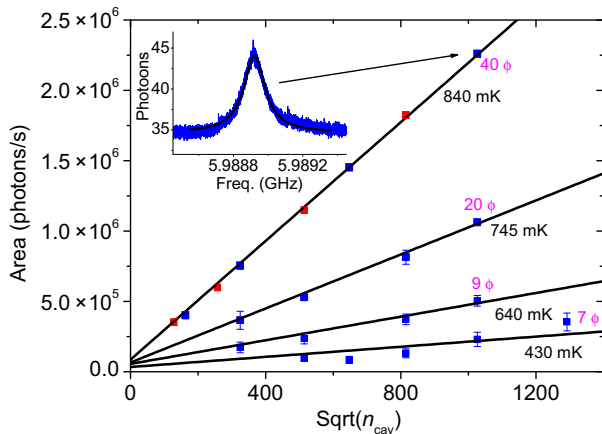
FIG. 13. Photon flux due to occupation of the cavity mode in excess of that expected from the cryostat temperature. The x axis is $\sqrt{n_{\rm cav}}$ (blue-detuned pump scheme for blue symbols, red-detuned pump for red). Inset: example of resonance peak obtained from spectrum analyzer. The lines are guides to the eye. The numbers in magenta correspond to the calculated intracavity population for the last point of each temperature series (from fit value of $\kappa_{\rm ext}$, see text).
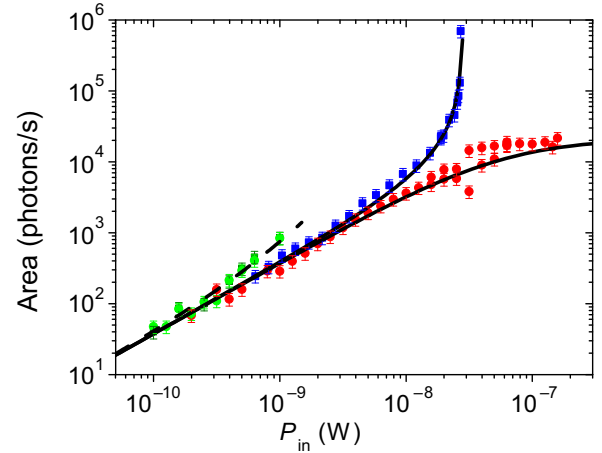
FIG. 14. Measured signal amplitude for the three schemes used at 210 mK: blue-detuned pump, red-detuned pump, and "in-cavity" (green, the square and circle symbols stand for Stokes and anti-Stokes peaks, respectively). For blue and red pumping, the fits correspond to Eqs. (1)–(4), defining the coefficient $\mathcal{M}$. The dashed line corresponds to the heating measured in Fig. 6.

theoretical expressions [19], we find out that this effect remains always negligible with respect to other problems creating the finite error bars of Fig. 7.

From the careful measurement of the cavity at each point, the knowledge of the heating effects in Figs. 6 and 13, we can guarantee that the experiment is performed in the best possible conditions. To be then quantitative, we finally need to be able to convert photon population in the Stokes and anti-Stokes peaks into phonon populations. To do so, we need to know the parameter $\mathcal{M}$ introduced in Eq. (1). In principle, one could calculate it from theory, knowing all experimental details of the setup [19]. However, since all of these parameters are known within some experimental error, the final value obtained for $\mathcal{M}$ is of poor precision. It is thus much more efficient to *calibrate it* at a given temperature: this is performed in Fig. 14, at sufficiently high $T_{\rm cryo}$ to guarantee a good thermal coupling and enough resolution in signal (210 mK). In this plot, we show the signal (area) obtained for the three schemes presented in Fig. 2, as a function of $P_{\rm in}$ (they thus all overlap at low powers). The lines are fit to theory Eqs. (3) and (4) [19], with the dashed one taking into account the heating produced by the large $n_{\rm cav}$ reached with the "in-cavity" scheme. We thus obtain $\mathcal{M} \approx 1.8 \times 10^{12}$ photons/s/W/K for our device. Note that at the highest powers used, in the red-detuned pumping scheme the mode cooled from 210 mK down to approximately 20 mK.

Our aim is to demonstrate the capabilities of the method for temperatures as low as possible and a coupling g_0, which is *not* especially large. We therefore relied on the out-of-plane flexure of our NEMS beam; in-plane and out-of-plane modes are both characterized first at room
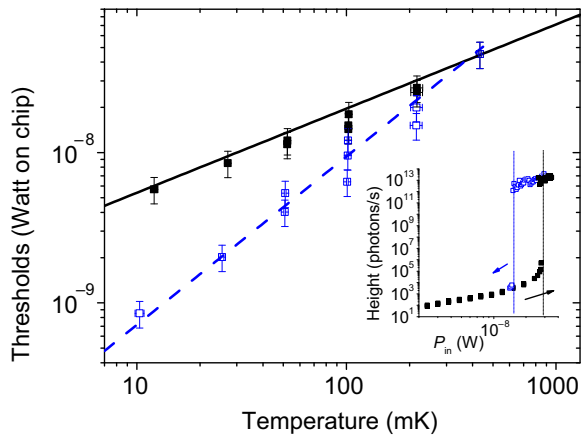
FIG. 15. Main: power threshold P_{thr} to self-oscillation regime (blue-detuned pump scheme). A large hysteresis is seen, certainly due to nonlinearities in the system. The black line is the calculated value $\propto \gamma_m$ from Eq. (3), and the dashed line is a guide to the eyes $\propto \gamma_m^2$. Inset: peak height measured sweeping the power up (full black), and down (empty blue symbols) at 210 mK. The dashed verticals are the threshold positions.

temperature using optics [69]. The out-of-plane flexural mode is found at 3.660 MHz, shifted about 280 kHz from the in-plane one. Both had a quality factor of about 6500. At low temperatures, the method then relies on the blue-detuned pump instability: below the threshold it enables *amplification* of the weak signal, and the position of the threshold itself gives access to the parameter γ_m needed for quantitative fits. It is thus, in principle, *not necessary* to be able to resolve the signal at low powers; in particular, in these conditions sideband-assymetry thermometry would be impractical.

The definition of γ_m from the threshold position is illustrated in Fig. 15. Ramping up the power, from Eq. (3) we can recalculate the damping rate from the position of the threshold P_{thr} (full symbols and full line). Furthermore, it happens that this threshold towards self-sustained oscillations is hysteretic (Fig. 15 empty symbols). This effect is not yet modeled, but it clearly arises from nonlinearities in the system. For microwave optomechanics, these are genuine *geometrical* nonlinearites, as opposed to thermal nonlinearities seen in optics [70]. The temperature dependence of the down-sweep threshold (large amplitude motion) is even stronger than for the up-sweep one (small amplitude). Again, no thermal decoupling can be seen down to 10 mK; the heating effect (Fig. 6) is taken into account, and has only a small impact on the data.

---

[1] A. N. Cleland and M. L. Roukes, Fabrication of high frequency nanometer scale mechanical resonators from bulk Si crystals, Appl. Phys. Lett. **69**, 2653 (1996).

[2] A. D. O'Connell, M. Hofheinz, M. Ansmann, Radoslaw C. Bialczak, M. Lenander, Erik Lucero, M. Neeley, D. Sank, H. Wang, M. Weides, J. Wenner, John M. Martinis, and A. N. Cleland, Quantum ground state and single-phonon control of a mechanical resonator, Nature **464**, 697 (2010).

[3] T. A. Palomaki, J. W. Harlow, J. D. Teufel, R. W. Simmonds, and K. W. Lehnert, Coherent state transfer between itinerant microwave fields and a mechanical oscillator, Nature **495**, 210 (2013).

[4] J.-M. Pirkkalainen, S. U. Cho, Jian Li, G. S. Paraoanu, P. J. Hakonen, and M. A. Sillanpää, Hybrid circuit cavity quantum electrodynamics with a micromechanical resonator, Nature **494**, 211 (2013).

[5] C. A. Regal, J. D. Teufel, and K. W. Lehnert, Measuring nanomechanical motion with a microwave cavity interferometer, Nat. Phys. **4**, 555 (2008).

[6] Alfredo Rueda, Florian Sedlmeir, Michele C. Collodo, Ulrich Vogl, Birgit Stiller, Gerhard Schunk, Dmitry V. Strekalov, Christoph Marquardt, Johannes M. Fink, Oskar Painter, Gerd Leuchs, and Harald G. L. Schwefel, Efficient microwave to optical photon conversion: An electro-optical realization, Optica **3**, 597 (2016).

[7] A. P. Higginbotham, P. S. Burns, M. D. Urmey, R. W. Peterson, N. S. Kampel, B. M. Brubaker, G. Smith, K. W. Lehnert, and C. A. Regal, Harnessing electro-optic correlations in an efficient mechanical converter, Nat. Phys. **14**, 1038 (2018).

[8] A. Metelmann and A. A. Clerk, Nonreciprocal Photon Transmission and Amplification via Reservoir Engineering, Phys. Rev. X **5**, 021025 (2015).

[9] Gabriel A. Peterson, Florent Q. Lecocq, Katarina Cicak, Raymond W. Simmonds, Jose A. Aumentado, and John D. Teufel, Demonstration of Efficient Nonreciprocity in a Microwave Optomechanical Circuit, Phys. Rev. X **7**, 031001 (2017).

[10] N. R. Bernier, L. D. Tóth, A. Koottandavida, M. A. Ioannou, D. Malz, A. Nunnenkamp, A. K. Feofanov, and T. J. Kippenberg, Nonreciprocal reconfigurable microwave optomechanical circuit, Nat. Comm. **8**, 604 (2017).

[11] S. Barzanjeh, M. Wulf, M. Peruzzo, M. Kalaee, P. B. Dieterle, O. Painter, and J. M. Fink, Mechanical on-chip microwave circulator, Nat. Comm. **8**, 953 (2017).

[12] E. E. Wollman, C. U. Lei, A. J. Weinstein, J. Suh, A. Kronwald, F. Marquardt, A. A. Clerk, and K. C. Schwab, Quantum squeezing of motion in a mechanical resonator, Science **349**, 952 (2015).

[13] C. F. Ockeloen-Korppi, E. Damskägg, J.-M. Pirkkalainen, M. Asjad, A. A. Clerk, F. Massel, M. J. Woolley, and M. A. Sillanpää, Stabilized entanglement of massive mechanical oscillators, Nature **556**, 478 (2018).

[14] Francesco Massel, Sung Un Cho, Juha-Matti Pirkkalainen, Pertti J. Hakonen, Tero T. Heikkilä, and Mika A. Sillanpää, Multimode circuit optomechanics near the quantum limit, Nat. Comm. **3**, 987 (2012).

[15] A. J. Weinstein, C. U. Lei, E. E. Wollman, J. Suh, A. Metelmann, A. A. Clerk, and K. C. Schwab, Observation and Interpretation of Motional Sideband Asymmetry in a Quantum Electromechanical Device, Phys. Rev. X **4**, 041003 (2014).

[16] A. D. Armour and M. P. Blencowe, Probing the quantum coherence of a nanomechanical resonator using a

superconducting qubit: I. Echo scheme, New J. Phys. **10**, 095004 (2008).

[17] Dustin Kleckner, Igor Pikovski, Evan Jeffrey, Luuk Ament, Eric Eliel, Jeroen van den Brink, and Dirk Bouwmeester, Creating and verifying a quantum superposition in a micro-optomechanical system, New J. Phys. **10**, 095020 (2008).

[18] Dustin Paul Kleckner, PhD thesis, University of California, Santa Barbara, (04/2010).

[19] Markus Aspelmeyer, Tobias J. Kippenberg, and Florian Marquardt, Cavity optomechanics, Rev. Mod. Phys. **86**, 1391 (2014).

[20] A. Shibahara, O. Hahtela, J. Engert, H. van der Vliet, L. V. Levitin, A. Casey, C. P. Lusher, J. Saunders, D. Drung, and Th. Schurig, Primary current-sensing noise thermometry in the millikelvin regime, Trans. R. Soc. A **374**, 20150054 (2016).

[21] R. Blaauwgeers, M. Blazkova, M. Clovecko, V. B. Eltsov, R. de Graaf, J. Hosio, M. Krusius, D. Schmoranzer, W. Schoepe, L. Skrbek, P. Skyba, R. E. Solntsev, and D. E. Zmeev, Quartz tuning fork: Thermometer, pressure- and viscometer for helium liquids, J. Low Temp. Phys. **146**, 537 (2007).

[22] A. K. Naik, M. S. Hanay, W. K. Hiebert, X. L. Feng, and M. L. Roukes, Towards single-molecule nanomechanical mass spectrometry, Nat. Nanotech. **4**, 445 (2009).

[23] M. A. Sillanpää, (private communication).

[24] Tristan Rocheleau, PhD thesis, Cornell University, (2011).

[25] K. Lehnert and J. Teufel, (private communication).

[26] J. D. Teufel, T. Donner, M. A. Castellanos-Beltran, J. W. Harlow, and K. W. Lehnert, Nanomechanical motion measured with an imprecision below that at the standard quantum limit, Nat. Nanotech. **4**, 820 (2009).

[27] T. Rocheleau, T. Ndukum, C. Macklin, J. B. Hertzberg, A. A. Clerk, and K. C. Schwab, Preparation and detection of a mechanical resonator near the ground state of motion, Nature **463**, 72 (2010).

[28] B. D. Hauer, P. H. Kim, C. Doolin, F. Souris, and J. P. Davis, Two-level system damping in a quasi-one-dimensional optomechanical resonator, Phys. Rev. B **98**, 214303 (2018).

[29] M. Defoort, K. J. Lulla, C. Blanc, H. Ftouni, O. Bourgeois, and E. Collin, Stressed silicon nitride nanomechanical resonators at helium temperatures, J. Low Temp. Phys. **171**, 731 (2013).

[30] C. Bäuerle, Y. Bunkov, S. N. Fisher, Chr. Gianese, and H. Godfrin, The new grenoble 100 microkelvin refrigerator, Czekoslovak J. Phys. **46**, 2791 (1996).

[31] Jasper Chan, T. P. Mayer Alegre, Amir H. Safavi-Naeini, Jeff T. Hill, Alex Krause, Simon Gröblacher, Markus Aspelmeyer, and Oskar Painter, Laser cooling of a nanomechanical oscillator into its quantum ground state, Nature **478**, 89 (2011).

[32] J. D. Teufel, Tobias Donner, Dale Li, J. W. Harlow, M. S. Allman, Katarina Cicak, A. J. Sirois, Jed D. Whittaker, K. W. Lehnert, and Raymond W. Simmonds, Sideband cooling of micromechanical motion to the quantum ground state, Nature **475**, 359 (2011).

[33] Florian Marquardt, J. G. E. Harris, and S. M. Girvin, Dynamical Multistability Induced by Radiation Pressure in High-Finesse Micromechanical Optical Cavities, Phys. Rev. Lett. **96**, 103901 (2006).

[34] T. J. Kippenberg, H. Rokhsari, T. Carmon, A. Scherer, and K. J. Vahala, Analysis of Radiation-Pressure Induced Mechanical Oscillation of an Optical Microcavity, Phys. Rev. Lett. **95**, 033901 (2005).

[35] V. Singh, S. J. Bosman, B. H. Schneider, Y. M. Blanter, A. Castellanos-Gomez, and G. A. Steele, Optomechanical coupling between a multilayer graphene mechanical resonator and a superconducting microwave cavity, Nat. Nanotech. **9**, 820 (2014).

[36] P. Mohanty, D. A. Harrington, K. L. Ekinci, Y. T. Yang, M. J. Murphy, and M. L. Roukes, Intrinsic dissipation in high-frequency micromechanical resonators, Phys. Rev. B **66**, 085416 (2002).

[37] F. Hoehne, Yu. A. Pashkin, O. Astafiev, L. Faoro, L. B. Ioffe, Y. Nakamura, and J. S. Tsai, Damping in high-frequency metallic nanomechanical resonators, Phys. Rev. B **81**, 184112 (2010).

[38] A. Venkatesan, K. J. Lulla, M. J. Patton, A. D. Armour, C. J. Mellor, and J. R. Owers-Bradley, Dissipation due to tunneling two-level systems in gold nanomechanical resonators, Phys. Rev. B **81**, 073410 (2010).

[39] K. J. Lulla, M. Defoort, C. Blanc, O. Bourgeois, and E. Collin, Evidence for the Role of Normal-state Electrons in Nanoelectromechanical Damping Mechanisms at Very low Temperatures, Phys. Rev. Lett. **110**, 177206 (2013).

[40] M. Hamoumi, P. E. Allain, W. Hease, E. Gil-Santos, L. Morgenroth, B. Gérard, A. Lemaître, G. Leo, and I. Favero, Microscopic Nanomechanical Dissipation in Gallium Arsenide Resonators, Phys. Rev. Lett. **120**, 223601 (2018).

[41] Gregory S. MacCabe, Hengjiang Ren, Jie Luo, Justin D. Cohen, Hengyun Zhou, Alp Sipahigil, Mohammad Mirhosseini, and Oskar Painter, Phononic bandgap nano-acoustic cavity with ultralong phonon lifetime, arXiv:1901.04129v1 (2019).

[42] M. C. Cross and Ron Lifshitz, Elastic wave transmission at an abrupt junction in a thin plate with application to heat transport and vibrations in mesoscopic systems, Phys. Rev. B **64**, 085324 (2001).

[43] J. Suh, A. J. Weinstein, C. U. Lei, E. E. Wollman, S. K. Steinke, P. Meystre, A. A. Clerk, and K. C. Schwab, Mechanically detecting and avoiding the quantum fluctuations of a microwave field, Science **344**, 1262 (2014).

[44] S. Barzanjeh, (private communication).

[45] Olivier Maillet, PhD thesis, Université Grenoble Alpes (25/05/2016).

[46] Olivier Maillet, Xin Zhou, Rasul R. Gazizulin, Bojan R. Ilic, Jeevak M. Parpia, Olivier Bourgeois, Andrew D. Fefferman, and Eddy Collin, Measuring frequency fluctuations in nonlinear nanomechanical resonators, ACS Nano **12**, 5753 (2018).

[47] Marc Sansa, Eric Sage, Elizabeth C. Bullard, Marc Gély, Thomas Alava, Eric Colinet, Akshay K. Naik, Luis Guillermo Villanueva, Laurent Duraffourg, Michael L. Roukes, Guillaume Jourdan, and Sébastien Hentz, Frequency fluctuations in silicon nanoresonators, Nat. Nanotech. **11**, 552 (2016).

[48] O. Maillet, F. Vavrek, A. D. Fefferman, O. Bourgeois, and E. Collin, Classical decoherence in a nanomechanical resonator, New J. Phys. **18**, 073022 (2016).

[49] M. Defoort, PhD thesis, Université Grenoble Alpes, (16/12/2014).

[50] C. Song, T. W. Heitmann, M. P. DeFeo, K. Yu, R. McDermott, M. Neeley, John M. Martinis, and B. L. T. Plourde, Microwave response of vortices in superconducting thin films of Re and Al, Phys. Rev. B **79**, 174512 (2009).

[51] A. B. Zorin, F.-J. Ahlers, J. Niemeyer, T. Weimann, H. Wolf, V. A. Krupenin, and S. V. Lotkhov, Background charge noise in metallic single-electron tunneling devices, Phys. Rev. B **53**, 13682 (1996).

[52] S. E. de Graaf, L. Faoro, J. Burnett, A. A. Adamyan, A. Ya. Tzalenchuk, S. E. Kubatkin, T. Lindström, and A. V. Danilov, Suppression of low-frequency charge noise in superconducting resonators by surface spin desorption, Nat. Comm. **9**, 1143 (2018).

[53] Jiansong Gao, Miguel Daal, John M. Martinis, Anastasios Vayonakis, Jonas Zmuidzinas, Bernard Sadoulet, Benjamin A. Mazin, Peter K. Day, and Henry G. Leduc, A semiempirical model for two-level system noise in superconducting microresonators, Appl. Phys. Lett. **92**, 212504 (2008).

[54] King Y. Fong, Wolfram H. P. Pernice, and Hong X. Tang, Frequency and phase noise of ultrahigh Q silicon nitride nanomechanical resonators, Phys. Rev. B **85**, 161410(R) (2012).

[55] Alexander Bilmes, Sebastian Zanker, Andreas Heimes, Michael Marthaler, Gerd Schön, Georg Weiss, Alexey V. Ustinov, and Jürgen Lisenfeld, Electronic decoherence of two-level systems in a Josephson junction, Phys. Rev. B. **96**, 064504 (2017).

[56] E. Nazaretski, R. D. Merithew, V. O. Kostroun, A. T. Zehnder, R. O. Pohl, and J. M. Parpia, Effect of Low-Level Radiation on the Low Temperature Acoustic Behavior of a-SiO$_2$, Phys. Rev. Lett. **92**, 245502-1 (2004).

[57] G. Pickett and C. Enss, The european microkelvin platform, Nat. Rev. Mater. **3**, 18012 (2018).

[58] N. S. Lawson, A simple heat switch for use at millikelvin temperatures, Cryogenics **22**, 667 (1982).

[59] R. Rusby *et al.*, in *Proceedings of TEMPMEKO*, edited by B. Fellmuth, J. Seidel, and G. Scholz (VDE Verlag GmbH, Berlin, 2002), Vols. 1 & 2.

[60] F. Pobell, *Matter and Methods at low Temperatures* (Springer-Verlag, Berlin Heidelberg, 1996), 2nd ed.

[61] A. M. Guénault, V. Keith, C. J. Kennedy, S. G. Mussett, and G. R. Pickett, The mechanical behavior of a vibrating wire in superfluid ^{3}He-B in the ballistic limit, J. Low Temp. Phys. **62**, 511 (1986).

[62] C. B. Winkelmann, E. Collin, Yu. M. Bunkov, and H. Godfrin, Vibrating wire thermometry in superfluid ^{3}He, J. Low Temp. Phys. **135**, 3 (2004).

[63] D. I. Bradley, M. Clovecko, S. N. Fisher, D. Garg, A. Guénault, E. Guise, R. P. Haley, G. R. Pickett, M. Poole, and V. Tsepelin, Thermometry in normal liquid He-3 using a quartz tuning fork viscometer, J. Low Temp. Phys. **171**, 750 (2013).

[64] D. I. Bradley, P. Crookston, S. N. Fisher, A. Ganshin, A. Guénault, R. P. Haley, M. J. Jackson, G. R. Pickett, R. Schanen, and V. Tsepelin, The damping of a quartz tuning fork in superfluid He-3-B at low temperatures, J. Low Temp. Phys. **157**, 476 (2009).

[65] Dieter Vollhardt and Peter Wolfle, *The Superfluid Phases of Helium 3* (Dover Books on Physics, New-York, 2013).

[66] D. C. Carless, H. E. Hall, and J. R. Hook, Vibrating wire measurements in liquid ^{3}He. I. The normal state, J. Low Temp. Phys. **50**, 583 (1983).

[67] D. C. Carless, H. E. Hall, and J. R. Hook, Vibrating wire measurements in liquid ^{3}He. II. The superfluid B phase, J. Low Temp. Phys. **50**, 605 (1983).

[68] M. S. Khalil, M. J. A. Stoutimore, F. C. Wellstood, and K. D. Osborn, An analysis method for asymmetric resonator transmission applied to superconducting devices, J. Appl. Phys. **111**, 054510 (2012).

[69] A room-temperature vacuum chamber equipped with a laser readout from O. Arcizet and B. Pigeau is used.

[70] Christophe Baker, Sebastian Stapfner, David Parrain, Sara Ducci, Giuseppe Leo, Eva M. Weig, and Ivan Favero, Optical instability and self-pulsing in silicon nitride whispering gallery resonators, Opt. Express **20**, 29076 (2012).